

Tree Roots Reconstruction Framework for Accurate Positioning in Heterogeneous Soil

Wen-hao Luo^{ID}, Student Member, IEEE, Yee Hui Lee^{ID}, Senior Member, IEEE, Hai-Han Sun, Lai Fern Ow, Mohamed Lokman Mohd Yusof^{ID}, and Abdulkadir C. Yucel^{ID}, Senior Member, IEEE

Abstract—Ground-penetrating radar has recently found wide application in the underground imaging of tree roots. However, ignoring the random and complex nature of the heterogeneous soil and assuming the soil’s relative permittivity constant throughout the survey region may yield an inaccurate tree root positioning. Meanwhile, the incompatible relative soil permittivity results in low image quality of the roots reconstruction. Furthermore, the soil’s spatial heterogeneity introduces unwanted environmental clutter in the mapping of the tree root. A data processing framework is proposed to address these issues for retrieving the tree roots in heterogeneous soil environments. The proposed framework combines four techniques to be applied consecutively: First, a hyperbola extraction method based on a column-connection clustering algorithm is used to extract individual hyperbolae in B-scans, eliminate mutual influence in the process, and suppress noise. Second, an improved Hough transform technique is adopted to estimate the equivalent permittivity of each root’s surrounding soil environment for each extracted hyperbola. Third, individual root restoration is done by transferring each hyperbola to a spot using its corresponding soil equivalent permittivity. Finally, individually restored features are combined in the final image. The images obtained via the proposed framework show a well reconstructed two-dimensional tree roots scenario. The applicability and the effectiveness of the proposed framework have been demonstrated through numerical simulations and field measurements.

Index Terms—Data processing framework, ground-penetrating radar (GPR), heterogeneous soil, two-dimensional (2-D) tree roots reconstruction.

I. INTRODUCTION

TREE roots absorb water and nutrients and maintain the trees’ growth [1]–[3]. Trees with unhealthy roots can easily fall, resulting in loss of lives and damage to properties [4]. Therefore, it is of critical importance to be able to map the tree roots and monitor their health. Many methods have been developed to investigate tree roots. Traditional methods, such as excavation and uprooting, are destructive, labor-intensive,

Manuscript received October 20, 2021; revised December 4, 2021; accepted February 12, 2022. Date of publication February 16, 2022; date of current version March 2, 2022. This work was supported by the Ministry of National Development Research Fund, National Parks Board, Singapore. (*Corresponding authors: Yee Hui Lee; Abdulkadir C. Yucel*).

Wen-hao Luo, Yee Hui Lee, Hai-Han Sun, and Abdulkadir C. Yucel are with the School of Electrical and Electronic Engineering, Nanyang Technological University, Singapore 639798 (e-mail: wen-hao.luo@ntu.edu.sg; eyh-lee@ntu.edu.sg; hannah.h.sun@outlook.com; acyucel@ntu.edu.sg).

Lai Fern Ow and Mohamed Lokman Mohd Yusof are with the National Parks Board, Singapore 259569 (e-mail: Genevieve_ow@nparks.gov.sg; mohamed_lokman_mohd_yusof@nparks.gov.sg).

Digital Object Identifier 10.1109/JSTARS.2022.3151869

and time-consuming, thus are not preferred in long-term studies [5], [6]. Recently, nondestructive techniques for tree root mapping have been receiving significant attention. Among these techniques, ground-penetrating radar (GPR), leveraging electromagnetic (EM) fields to detect changes in the relative permittivity of the media, has been widely used [7], [8]. Some studies have successfully employed the GPR to estimate parameters related to roots, such as the root diameter [9], [10], root orientation [11], and root biomass [12], [13]. The limitations of the GPR for root detection under different environments have also been investigated [14].

The raw data obtained by GPR needs to be processed and interpreted carefully: first, the raw data is preprocessed using a variety of techniques. The time-zero correction is used to fix the position of the reflection of the air-ground interface as common time-zero position [15]. The band-pass filtering is employed to improve the signal-to-noise ratio (SNR) by filtering out the signal components with frequencies outside the operating bandwidth [16]. The gain-compensation function is applied to assist in data display and interpretation [17]. Second, horizontal clutter due to the direct coupling between antennas and reflection from the ground surface is suppressed via background removal methods such as the mean subtraction [18], the principal component analysis [19], and singular value decomposition (SVD) [20]. Third, the soil’s relative permittivity is obtained by a hyperbola fitting method [21] or by using a dielectric probe to calculate the EM wave’s speed in the soil. Finally, the data undergoes a scenario retrieval process to restore the scenario.

Several processing techniques on tree roots detection have been proposed [22], [23], these are referred to as conventional frameworks. These frameworks consider the soil’s relative permittivity as a constant (same medium velocity) throughout the survey site and use the measured or estimated permittivity at a specific location to map the entire underground environment. Some widely used commercial GPR systems, such as Aladdin hand-held dual-polarized antenna from IDS Georadar [24] and GSSI subsurface interface radar System [25], requires users to input a constant medium permittivity value. The soil’s heterogeneity affects the EM waves’ speed significantly at different parts of the soil. This is especially so in tropical areas where humidity is high. Assuming a constant soil permittivity therefore significantly affects the accuracy of these techniques. In [25], [26], a realistic scenario where the vertical and/or horizontal permittivity varies (heterogeneous medium) has been reported. In [26], researchers introduced an

equivalent permittivity function which is computation intensive, and it assumes that the soil is horizontally homogeneous. In [27], frequency-wavenumber modeling and migration of two-dimensional (2-D) GPR data is presented for either horizontally layered medium or laterally heterogeneous medium. The targets are pipes, and the distance between two pipes is far.

To the best of our knowledge, methods that deal with roots buried close to each other under spatially heterogeneous soil environment have not been reported. According to [28], [29], when particles density (ρ_s) = 2.66 g/cm³, bulk density (ρ_b) = 2 g/cm³, sand fraction (S) = 0.1, clay fraction (C) = 0.9, and for water volumetric fraction (f_u) = 0.05–0.2 with a step of 0.05, the real part of the relative permittivity of the soil varies from 5 to 13 with a step of around 2.5 across the frequency range of interest for landmine detection (0.5–3.0 GHz), and when S = 0.9, C = 0.1, the relative permittivity varies from 8 to 22 with a step of about 5. It can be concluded that the relative permittivity of the soil at different locations on the same piece of land may vary drastically due to the different water content, composition, and density. Processing the GPR data using the same relative permittivity may lead to inaccurate estimation of the targets' horizontal and vertical positions. The reconstruction of the targets using incompatible permittivity leads to a misinterpretation of the scenario. Besides, the heterogeneity of the soil causes interference which disguises the signals reflected by the roots. Therefore, it is imperative to explore an effective and accurate method to improve detection accuracy and minimize clutter noise in the images generated for heterogeneous soil environments.

In this article, a framework is proposed that reconstructs each root individually with its own surrounding medium velocity, the velocity is calculated using a vertical equivalent permittivity of the medium between the antenna and the root. The framework first preprocesses the B-scan via a column-connection clustering (C3) algorithm to extract hyperbolae [30]. In this process, the hyperbolae representing different tree roots are separated and extracted into new B-scans while removing the random clutter noise. Next, an improved Hough transform (IHT) method [31] is used to estimate the vertical equivalent soil permittivity and the root's position for each extracted hyperbola in the B-scans. By using the vertical equivalent permittivity of each root instead of treating the permittivity for the whole site as a constant, the reconstructed image of each root is obtained. All the reconstructed features are then combined in the final image with a unified depth resolution. The process of the individual hyperbola extraction, sequential processing of each signature, and image recombination is the main contribution of this article.

II. DATA PROCESSING FRAMEWORK AND METHODOLOGIES

The flowcharts of the conventional and the proposed frameworks are shown in Fig. 1(a) and (b), respectively. Both frameworks are capable of processing measurement data and the synthetic data obtained via simulations. The input of the frameworks is the B-scan obtained after preprocessing, which includes the time-zero correction [15], band-pass filtering [16], background

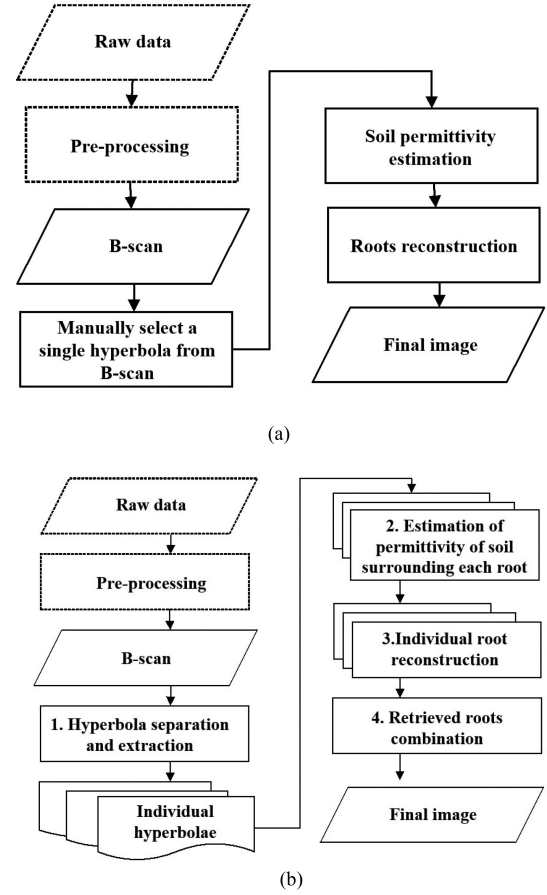


Fig. 1. (a) Conventional data processing framework. (b) Proposed data processing framework for retrieving tree roots in heterogeneous soil.

removal with SVD [20], and adaptive threshold [30]. In the conventional framework Fig. 1(a), a hyperbola corresponding to a tree root reflection at a specific location is manually selected to extract the soil permittivity. The extracted permittivity is then used to process the B-scans in the entire survey field. In this framework, the variation of soil permittivity at different locations in the survey site is not considered. Furthermore, the manual selection procedure requires users' intervention.

In the proposed framework in Fig. 1(b), the hyperbolae representing reflections from different roots are separated and extracted with minimal user intervention. Then, for each extracted hyperbola, its vertical equivalent permittivity is estimated and used in root retrieval. Note that each root will have its own vertical equivalent permittivity. This step takes the soil's heterogeneity into account, significantly improving the positioning accuracy for tree roots. Finally, the individual tree root images are combined to obtain the underground scenario. The technical components implemented in the proposed framework are described as follows.

A. Hyperbola Separation and Extraction

The purpose of this component in the framework is to extract each hyperbola from B-scans. The extracted hyperbolae can then be analyzed separately to reduce interference from intersecting regions and reduce environmental noise. Many researchers have

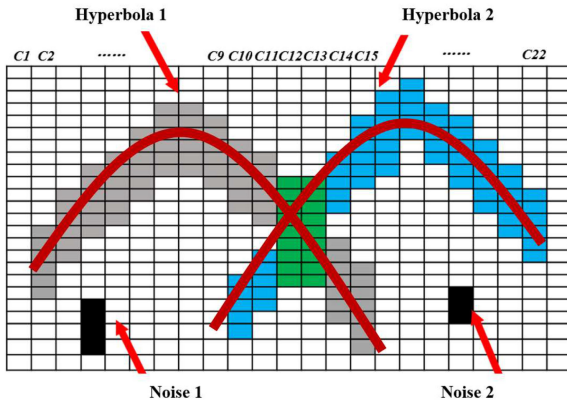


Fig. 2. Illustration of a B-scan with two regions of interest (hyperbolae 1 and 2) and noise. The implemented C3 algorithm can extract the hyperbolae 1 and 2 separately while ignoring the noises 1 and 2.

made surveys on detection of reflection hyperbolae with or without priori knowledge of the Medium [21], [30]. The method adopted here is the column-connection clustering (C3) algorithm [30]. For a B-scan shown in Fig. 2, the C3 algorithm extracts the hyperbolae 1 and 2 separately while ignoring noise 1 and 2.

To ease the description, a set of adjacent pixels in each column is named as a segment, such as the colored block in each column in Fig. 2. Segments with pixels less than a user-defined value s (e.g., 5 in Fig. 2) are regarded as noise, such as noise 1 (4 pixels) and 2 (3 pixels). According to [30], s is dependent on the sensor's noise level, the radar central frequency, and the sampling frequency. The maximum value of s is proportional to the sampling frequency f_s and inversely proportionate to the central frequency f_c . Ideal pixels of a segment s should be more than the pixel number of most of the noise, but less than the maximum value, $k \cdot f_s / f_c$ (k is a constant), in order to reject most of the noise.

By scanning from the first column C1 to the last column C22, adjacent segments in the connected columns are clustered into regions following several rules.

- 1) New regions are started from segments with no adjacent segment in the previous column, which are the gray segment in C2 and the blue segment in C10.
- 2) A segment is added into a region when it has connected pixels with the region, such as the gray segment in C10 is added to the gray region from C2 to C9.
- 3) Once more than one segment in the scanned column has connected pixels to a region (such as the blue and gray segments in C14 are connected to the green segment in C13), the region is separated into two regions to continue clustering.
- 4) A region stops extending when no segment in the next column has connected pixels to it (e.g., the gray segment in C15 and the blue segment in C22).

In the clustering process, coordinates of pixels in each region are recorded. By extracting the pixel coordinates and corresponding values in the original B-scan, a hyperbola is separated and extracted.

In the algorithm, two more thresholds should be set to reduce unwanted regions. First, when the connected pixels between a

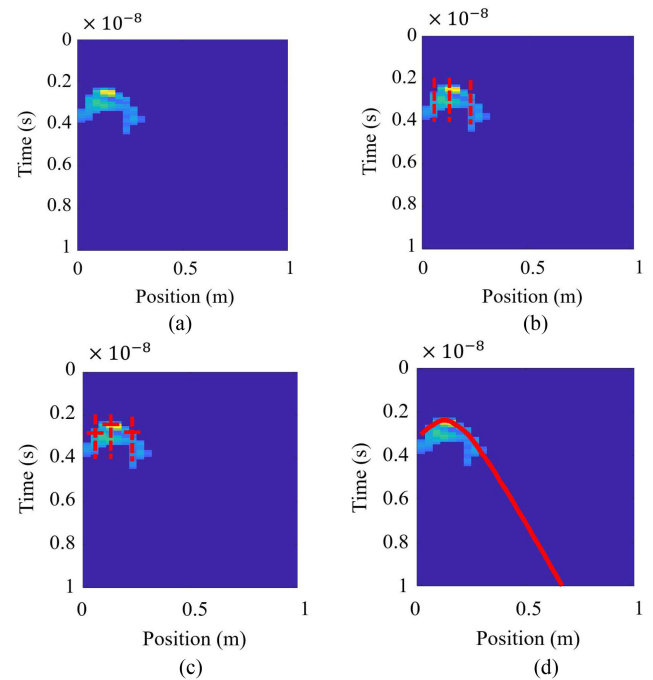


Fig. 3. Demonstration of a B-scan processed with IHT. (a) Hyperbola extracted by the C3 algorithm. (b) Randomly select three column indices. (c) Select row indices corresponding to the maximum pixel value in the selected columns. (d) Fitted hyperbola is shown as the red line.

segment and a region are less than a threshold, the region should stop extending. Second, when the number of pixels of a region is less than a threshold, the region is identified as noise and ignored. The setting of the thresholds is related to the experimental scene and system parameters, details of choosing the threshold are mentioned in [21] and [30].

B. Estimation of the Soil Equivalent Permittivity of Each Root

After extracting each hyperbola representing the reflection from a root, IHT is used to estimate the soil equivalent permittivity above each root. The detailed process of the IHT technique is demonstrated in Fig. 3 using a B-scan obtained in a field experiment.

The conventional Hough transform [31] uses a three-parameter parabolic equation to fit an extracted hyperbola, which is expressed as

$$\frac{t^2}{a^2} - \frac{(x - x_0)^2}{b^2} = 1 \quad (1)$$

where

$$a = t_0 \text{ and } b = \frac{t_0}{2} \frac{c}{\sqrt{\varepsilon_r}}. \quad (2)$$

where t is the two-way travel time of signals, and x is the horizontal position along the scanning trace. (x_0, t_0) denotes the center of the hyperbola, c is the speed of light in free space, and ε_{eq} is the soil's relative permittivity. In this article, the root diameter is ignored as it is usually small compared to the wavelength [32], detailed in Section III-A. The Hough transform

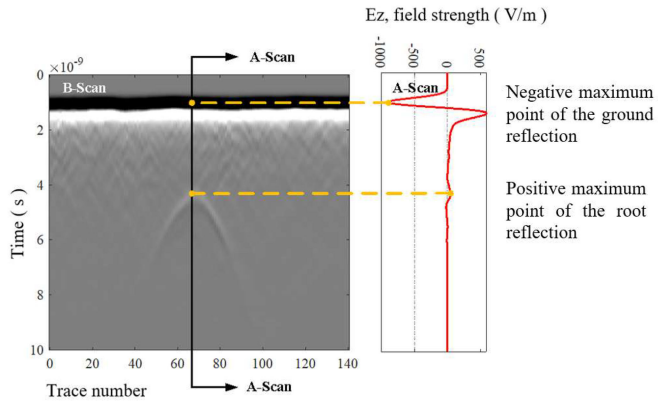


Fig. 4. Signal oscillating behavior and interpretation in a GPR scan image.

allows estimating the soil's relative permittivity as well as the depth and horizontal position of an object [32], [33].

To solve the unknown parameters a , b , and x_0 in (1), three different columns x_k are randomly selected in the region matrix in Fig. 3(b), and the row t_k corresponding to the largest pixel value in each selected column is chosen in Fig. 3(c). Using the three pairs of two parameters (x_k, t_k) , a set of (a, b, x_0) is derived. By iterating the process, multiple sets of the parameters are calculated. The iteration stops when the variation of averaged values is less than 0.1%, and the hyperbola is fitted using the averaged values of (a, b, x_0) , and the soil equivalent permittivity, depth, and horizontal position are extracted. In the IHT, the largest pixel value in each selected column is chosen due to the following reason. In each A-scan, the signal oscillates when the wave is reflected at the interface between air and soil and between soil and root. In practice, either the negative or positive maximum peaks of the wavelet or the zero-amplitude points between these two peaks can be used as the reference points for an oscillation. As illustrated in Fig. 4, the peaks of the absolute value of the wavelet were chosen as stable reference points. The negative maximum point of the ground reflection is set as reference time-zero position.

The effectiveness of IHT is evaluated using multiple sets of simulation results in different heterogeneous soil environments. Accurate estimation of soil's equivalent permittivity and objects' depths and horizontal positions will be presented in Section III-B.

C. Scenario Retrieval

Although the output of hyperbola fitting is acceptable for targets' center determination, the detection of the targets (e.g., tree roots) through B-scan requires a visually focused and accurate reconstruction. Many reconstruction techniques are applied to reconstruct the underground scenario. Such as migration methods [34]–[36], back projection [37], [38], and microwave tomographic inversion [39], [40]. All these reconstruction approaches require an accurate estimation of the wave propagation velocity in the medium, i.e., the accurate equivalent dielectric permittivity of the soil. Therefore, the accurate estimation of the equivalent soil permittivity for each root in a heterogeneous soil environment above is crucial.

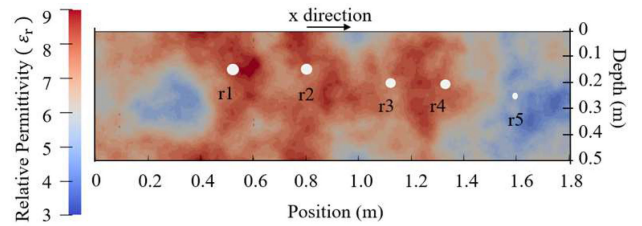


Fig. 5. Side view of the simulation scenario, where r_1 to r_5 are cylinders representing five roots. The soil's relative permittivity around r_5 is significantly different from that around the other four roots.

Migration, which was initially introduced in seismic surveys [41], has been successfully extrapolated to GPR [42]. From landmine detection [25], [43] to surface profiling [44], and target detection in multilayered scenarios [45], migration is a popular technique in the GPR application primarily due to its accuracy and minimum computational requirements. The F-K migration transforms an unfocused space-time GPR image into a focused image showing the object's true location with the corresponding EM reflectivity. The F-K migration is adopted here to focus the hyperbolae, the hyperbolae are extracted from the preprocessed B-scan through the method in Section II-A, the velocity of the host medium corresponds to each target is achieved through the method in Section II-B. The F-K migration is applied in both the proposed framework and the conventional framework to fairly compare their performance.

The comparison of different reconstruction approaches for landmine detection was reported in [25]. Reconstruction approaches comparison in tree roots application is an interesting topic that can be investigated in future research.

III. NUMERICAL EXPERIMENTS

A. Simulation Scenario

The numerical simulation of tree roots in a heterogeneous soil environment is carried out by an open-source gprMax software [46], which uses the finite-difference time-domain technique to characterize the transient EM phenomena. The spatial discretization step Δl set in the simulation is 0.002 m. The underground scenario is to simulate a simplified root system where several roots with different radius are buried at different depths in the heterogeneous soil. The simulation scenario is shown in Fig. 5. Five roots r_1 – r_5 are modeled with different radius. From left to right along the position axis, the first two roots are the thickest while the last one is the thinnest. The radius and depth of $r_1(r_2)$, $r_3(r_4)$, and r_5 are 2 and 16 cm, 1.6 and 20 cm, 1.3 and 25 cm, respectively. The roots have a volumetric water content of 50% with a relative permittivity of $\epsilon_{\text{root}} = 24$ and an electrical conductivity of $\sigma_{\text{root}} = 0.63$ mS/m for numerical simulation purpose [47], [48]. The magnetic permeability and magnetic conductivity are set to 1 and 0, respectively.

Parameters of heterogeneous soil are set by using the existing Peplinski model which leverages on the semi-empirical model [49], [50] and the fractal model [51] in gprMax. In the simulation, the soil has a sand fraction (S) of 0.3, a clay fraction (C) of 0.7, a sand particles density (ρ_s) of 2.66 gr/cm³, a bulk density

(ρ_b) of 2 gr/cm³, and a water volumetric fraction (f_u) that varies from 0.01 to 0.15. The number of soil elements and the fractal dimension (β) are set to be 20 and 1.5, respectively. As shown in Fig. 5, different colors indicate the relative permittivity of the soil [49]. To better verify the effectiveness of the processing framework, the positioning accuracy of the proposed framework is used in five different heterogeneous soil environments with the same roots' arrangement. The different soil environments have different sand fraction (S), clay fraction (C), and the water volumetric fraction (f_u), as given in Section III-B. Equivalent permittivity value (medium velocity) of each root is estimated, and the detection errors of the roots' depth and horizontal position by the proposed framework and the conventional framework are listed and compared, and the proposed framework is shown to perform better. The side views for the soil scenario are shown in Fig. 5.

In addition, to demonstrate the robustness of the proposed framework, three more sets of different tree root layouts in the same soil environment ($S = 0.3; C = 0.7; f_u = [0.01-0.15]$) are used. The side view of the roots in different cases was restored by both our proposed framework and the conventional framework. The comparison results are presented in Section III-B.

The above scenarios were simulated using a bi-static model with the polarization of source and probe parallel to the roots' longitudinal dimension. The source and probe are placed 0.10 m apart and are placed above the soil surface at a height of 0.05 m. The excitation waveform is a Ricker pulse with a central frequency of 1 GHz. The source and probe are moved along a trace along the x-direction (see Fig. 5) with a stepping of 0.01 m. 180 A-scans are collected and combined into a B-scan.

In our simulation, the center frequency is 1 GHz, the wavelength is approximately 10 cm for soil permittivity of around 6 to 8. As mentioned in Section II-B, the IHT adopted in this article is accurate in permittivity estimation when the root diameter is small relative to the wavelength [32]. When the diameter of the coarse root is close to 10 cm, the permittivity estimation would be inaccurate. Therefore, the center frequency will need to be reduced but the resolution will suffer. The cylindrical targets' radii and its relationship to frequency are detailed in [21].

B. Numerical Results

The proposed framework is implemented to process the B-scan obtained for the numerical scenarios described in Section III-A. The step-by-step processing results of the first scenario in Fig. 5 are shown in Figs. 7–11 to illustrate the workflow of the framework.

Fig. 6 illustrates the time-zero correction performed to set a common time-zero position. In Fig. 6(a), only oscillation caused by antenna-to-antenna separation and ground reflection is shown when there are no subsurface objects buried. In Fig. 6(b), the oscillation caused by antenna-to-antenna separation and ground reflection is at the same point as in Fig. 6(a), and there is another reflection caused by underground targets reflection. In Fig. 6(c), the A-scan is time-zero corrected by setting the negative maximum point of the ground reflection as shown in Fig. 6(a) and (b) as the time-zero position.

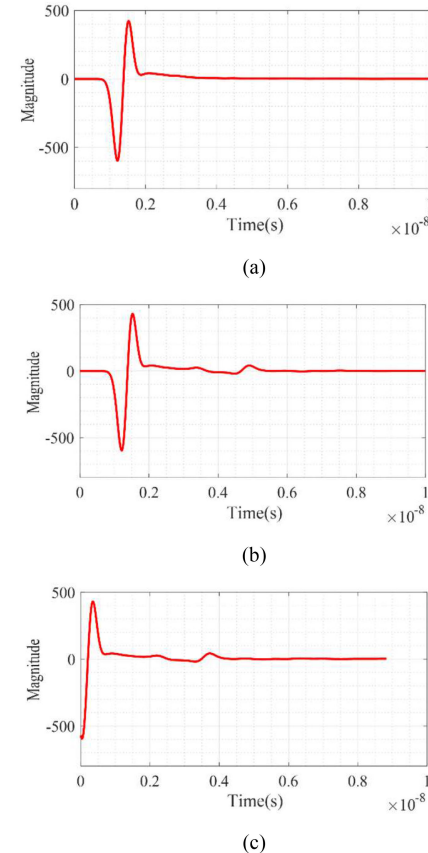


Fig. 6. A-scans of (a) raw data with no reflection from the targets. (b) Raw data with a reflection from the target. (c) Data with reflection from the target through time-zero correction.

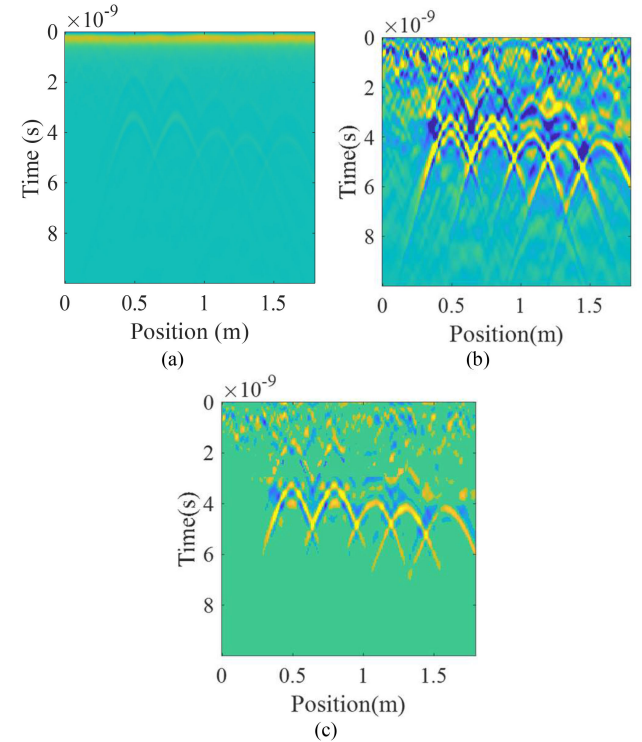


Fig. 7. (a) Time-zero corrected raw B-scan. (b) B-scan after SVD. (c) B-scan after preprocessing techniques.

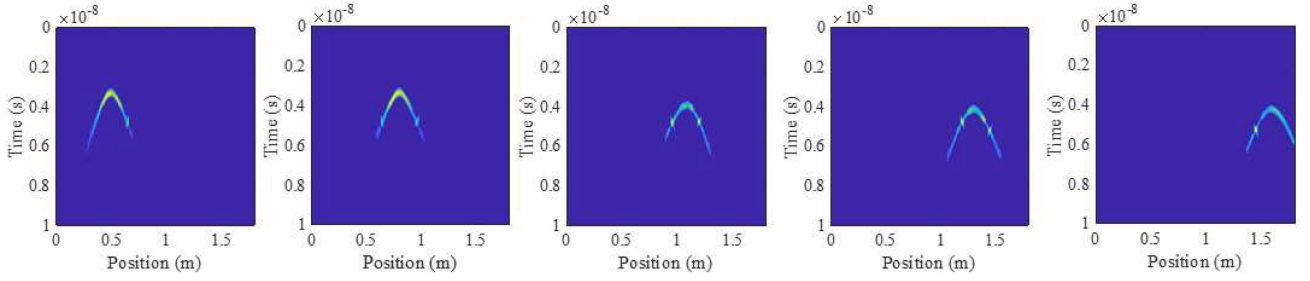


Fig. 8. Five hyperbolae extracted from the B-scan in Fig. 7(c) using the hyperbola extraction method. Each hyperbola will be treated as an ROI in the subsequent processing.

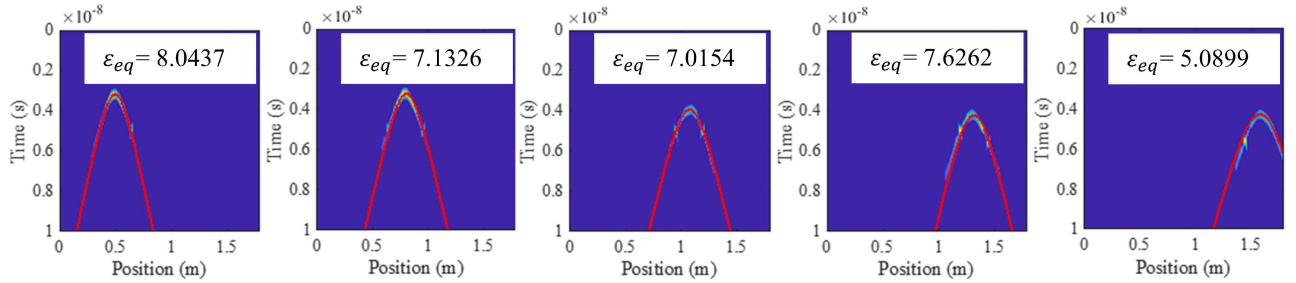


Fig. 9. Soil equivalent permittivity estimated by IHT for each ROI shown in Fig. 8. The depth and the horizontal position for each hyperbola are also estimated by IHT.

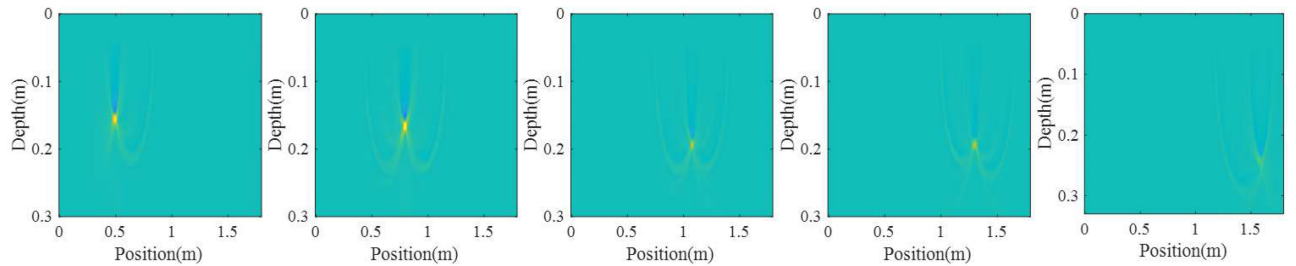


Fig. 10. Retrieval of each root.

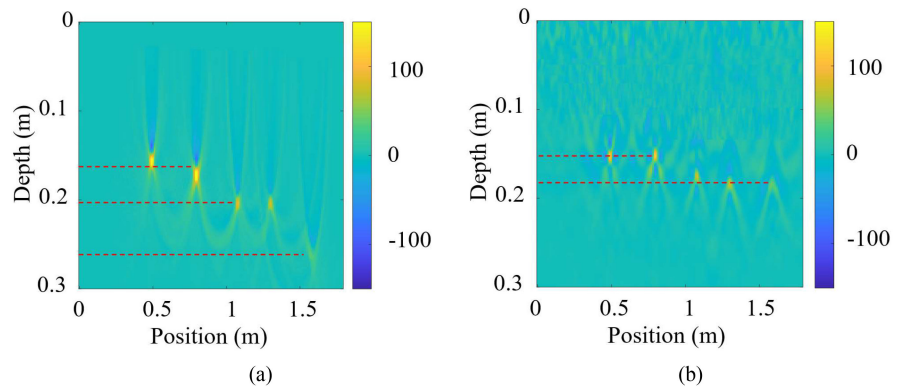


Fig. 11. Reconstructed scenario from (a) the proposed framework and (b) the conventional framework where data is dealt with constant soil permittivity = 8.0437.

Figs. 7(a) and (b) shows the time-zero corrected raw B-scan and the preprocessed B-scan using the SVD-based background removal method and the adaptive threshold technique, respectively. As shown in Fig. 7(a), after the time-zero correction, the direct coupling between two dipoles and the reflection caused by air/soil interface have large amplitude in raw data, forming a bright horizontal banding, and making the root reflection indistinguishable. As shown in Fig. 7(b), the surface reflection and coupling between Tx and Rx are mitigated after background removal. In this scenario, the three dominating singular values are excluded in SVD process to achieve a satisfactory background removal result. Because of the soil heterogeneity and high attenuation of EM waves in a moisturized environment, the reflections from the roots are merged with the background noise Fig. 7(b). Therefore, we further mitigate the noise using the adaptive threshold technique. After that, the five intersecting hyperbolae representing reflections of five roots are revealed, but still some noise is interfering [see Fig. 7(c)].

In the heterogeneous soil shown in Fig. 5, the relative permittivity of soil surrounding root $r5$ is significantly smaller than that of the other four roots. Using a single relative permittivity value to image the objects in the entire survey area, which is adopted in the conventional framework, can lead to inaccurate detection results. To overcome this limitation, in our framework, the hyperbola extraction method is used to extract the five hyperbolae individually. The extracted individual hyperbolae from Fig. 7(c) are shown in Fig. 8. Each hyperbola will be treated as a region of interest (ROI) in the subsequent processing. In addition, the threshold applied in the hyperbola extraction method further reduces the background noise, producing a B-scan with a clear object reflection.

Then, IHT is applied to each ROI to estimate the corresponding equivalent permittivity of surrounding soil. The estimation results are shown in Fig. 9. The estimated equivalent permittivity of the soil ($\hat{\varepsilon}_{eq}$) in the fifth picture is significantly smaller than that of the other four pictures, and the relative permittivity values of the other four pictures are similar, which is consistent with the simulated scenario shown in Fig. 5.

The average value of the five estimated relative permittivity ($\hat{\varepsilon}_{eq}^{ave}$) is 6.9. In the gprMax simulation, the heterogeneous soil (with $S = 0.3$, $C = 0.7$, $\beta = 1.5$) has the relative permittivity ranging from 3.7 to 8.2 with an average value ($\hat{\varepsilon}_{act}^{ave}$) of 6.02. The square error between the estimated average value and the true value is 2.6%.

The IHT also estimates the depth and horizontal position of each root. The accuracy of the depth and position estimation is evaluated by the root-mean-square relative error (RMSRE) which is defined as

$$\text{RMSRE} = \sqrt{\frac{1}{n} \sum_{i=1}^n \left(\frac{p_{\text{root},i}^{\text{act}} - p_{\text{root},i}^{\text{est}}}{p_{\text{root},i}^{\text{act}}} \right)^2}, \quad (3)$$

where $p_{\text{root},i}^{\text{act}}$ and $p_{\text{root},i}^{\text{est}}$ denote the actual depth/horizontal position and the estimated depth/horizontal position of the i^{th} root, respectively, and n is the number of buried roots. In this case, the RMSRE values of depths and horizontal position are 4.8% and 1.5%, respectively.

Afterward, each hyperbola is recovered with the corresponding soil equivalent permittivity. The results are shown in Fig. 10. In this step, the y-axis is transformed from time to depth. Five focused points are generated, and their depths and horizontal positions agree well with the calculated depths and positions via IHT.

In the final stage, the five focused points are combined into one image. In Figs. 7–9, the resolution of the y-axis is a time step Δt , and the corresponding resolution in depth Δd is calculated by

$$\Delta d = \frac{c\Delta t}{2\sqrt{\varepsilon_r}}. \quad (4)$$

As soil at different root locations has different relative permittivity, the depth resolution of each image in Fig. 10 is different. Therefore, an interpolation process is carried out to equalize the depth resolution to a target value for images in Fig. 10 before the image combination process. First, the target depth resolution Δd_1 (in this example, it is 10-4 m) is set. The matrix columns representing the initial depth resolution Δd_0 corresponding to each extracted hyperbola known in advance. Through the “nearest” interpolation method, the initial depth resolution Δd_0 is mapped to the target depth resolution Δd_1 . As shown in Fig. 11(a), the proposed framework well restores the simulated scenario of Fig. 5 where a shallower root with a larger radius corresponds to a brighter and bigger point. The depth and horizontal positions of the five roots are also estimated very accurately by the proposed framework.

To show the advantages of our framework over the conventional framework, the result processed through the proposed frame is compared with the results processed through the conventional framework. The comparison results are shown in Fig. 11. In the conventional framework, the relative permittivity of the soil surrounding root $r1$ is used to estimate all roots’ positions. Compared with Fig. 11(b), the proposed framework restores the simulation scenario with higher accuracy Fig. 11(a). To be specific, in Fig. 11(b), the root $r5$ appears at a similar depth to the root $r4$. However, it is buried at a deeper location in the simulation scenario. Our proposed framework, Fig. 11(a), restores the scenario with roots accurately positioned. The error in the depth estimation in Fig. 11(b) demonstrates the limited capability of using constant permittivity in roots position estimation in heterogeneous soil. Moreover, compared with the image generated by the conventional framework, our proposed framework produces a clearer image with less noise. The comparison of Fig. 11(a) and (b) verifies the effectiveness of the proposed framework in improving the detection accuracy of underground tree roots and reducing GPR image noise.

Six supplementary simulation scenarios are carried out with gprMax to investigate the applicability of the proposed framework in different heterogeneous soil environments. The layout of roots is the same as the one shown in Fig. 5, but the background soil contents are modeled with different compositions and moisture levels, the proportions of sand (S) and clay (C), and water volumetric fractions (f_u) of the soils are given in Table I. After preprocessing, B-scan data are further processed by our framework. The soil equivalent permittivity values are

TABLE I
ESTIMATED SOIL EQUIVALENT PERMITTIVITY FOR EACH ROOT IN EACH SOIL ENVIRONMENT R1–R5 ARE ROOTS1 TO ROOT5 IN THE SCENARIO

	$f_u = [0.01 - 0.1]$		$f_u = [0.01 - 0.15]$		$f_u = [0.01 - 0.2]$	
	$S = 0.3; C = 0.7$	$S = 0.7; C = 0.3$	$S = 0.3; C = 0.7$	$S = 0.7; C = 0.3$	$S = 0.3; C = 0.7$	$S = 0.7; C = 0.3$
R1	6.04	8.15	8.04	9.35	9.50	10.20
R2	5.75	6.14	7.13	7.93	7.72	9.53
R3	5.96	6.69	7.01	7.62	9.72	7.03
R4	6.05	7.56	7.62	8.70	8.44	7.80
R5	5.32	6.45	5.08	8.10	8.04	9.44
$\hat{\epsilon}_{act}^{ave}$	5.24	6.10	6.02	6.90	7.00	7.80

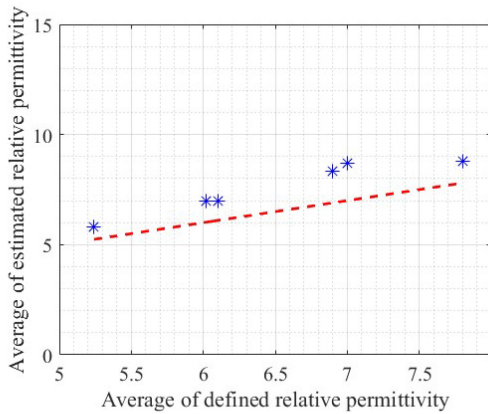


Fig. 12. Results of soil relative permittivity estimation of the six different soils with same layout of roots using the IHT method. The blue Asterisks corresponds to averaged estimated relative permittivity $\hat{\epsilon}_{act}^{ave}$ and red dotted line indicates the averaged defined relative permittivity $\hat{\epsilon}_{act}^{ave}$ of the six soil environments.

TABLE II
RMSE OF DEPTH ESTIMATION FOR PROPOSED FRAME (P) AND CONVENTIONAL FRAME (C)

Soil composition	water volumetric fraction f_u					
	[0.01 – 0.1]		[0.01 – 0.15]		[0.01 – 0.2]	
	P	C	P	C	P	C
($S = 0.3; C = 0.7$)	5.6%	11.3%	4.8%	10.2%	9.3%	12.0%
($S = 0.7; C = 0.3$)	8.5%	11.7%	5.5%	11.9%	10.0%	12.0%

estimated for each root in each scenario, as given in Table I. The average value ($\hat{\epsilon}_{eq}^{ave}$) is calculated. The comparison between $\hat{\epsilon}_{eq}^{ave}$ and the average value of actual soil relative permittivity ($\hat{\epsilon}_{act}^{ave}$) is shown in Fig. 12. $\hat{\epsilon}_{eq}^{ave}$ is positively correlated with $\hat{\epsilon}_{act}^{ave}$ with an averaged RMSRE value of 15.55%. The estimation accuracy is reasonable as the soil compositions are randomly distributed.

Tables II and III present the comparison of RMSRE values for the depths and horizontal positions estimated using our proposed framework and the conventional framework in the supplementary scenarios. As given in Table II, the RMSRE of

TABLE III
RMSE OF HORIZONTAL POSITION ESTIMATION FOR PROPOSED FRAME (P) AND CONVENTIONAL FRAME (C)

Soil composition	water volumetric fraction f_u					
	[0.01 – 0.1]		[0.01 – 0.15]		[0.01 – 0.2]	
	P	C	P	C	P	C
($S = 0.3; C = 0.7$)	1.4%	2.1%	1.5%	1.2%	1.1%	0.9%
($S = 0.7; C = 0.3$)	1.5%	1.4%	1.1%	2.1%	1.2%	1.4%

depth estimation is less than 10% in all cases using the proposed framework. For the root depth ranging from 10 to 20 cm, the difference between the predicted value and the actual value is only around 1 to 2 cm. However, the difference between the real and estimated depths can be higher than 5 cm in the conventional framework. In such a case, the RMSRE of depth estimation is more than 10% and much higher than that achieved by our proposed framework.

When the water content increases, due to the attenuation of EM waves and the increase of soil heterogeneity, part of the signal information is lost, this results in an increased RMSRE of the proposed framework. Nevertheless, the RMSRE is still within 10%, verifying the applicability of the proposed framework for different soil environments. As GPR is a downward detection system, the estimation of horizontal position is hardly affected by the unevenness of the soil surface. Therefore, as given in Table III, the similar estimation accuracy is achieved by both the proposed framework and the conventional framework. Due to the unavoidable errors in data processing (e.g., the time zero correction error, the estimation error of EM wave velocity in the soil, the depth interpolation error), the RMSRE of estimated depths will always be larger than the RMSRE of estimated horizontal positions.

Result of one of the supplementary experiments ($S = 0.3; C = 0.7; f_u = [0.01-0.2]$) processed by our framework and the conventional framework where radargrams are focused with the same permittivity are compared in Fig. 13. From the perspective of restoring the realistic scenario in Fig. 5, our proposed framework outperforms in the accuracy of root depth estimation in

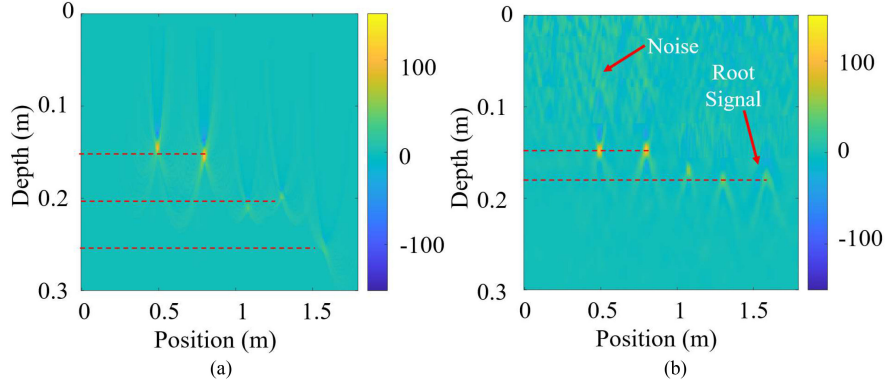


Fig. 13. The reconstructed scenario under a high moisture clay scenario: $S = 0.3$; $C = 0.7$; $f_u = [0.01-0.2]$ of (a) the proposed framework and (b) the conventional framework in which data are processed with constant soil permittivity = 9.53.

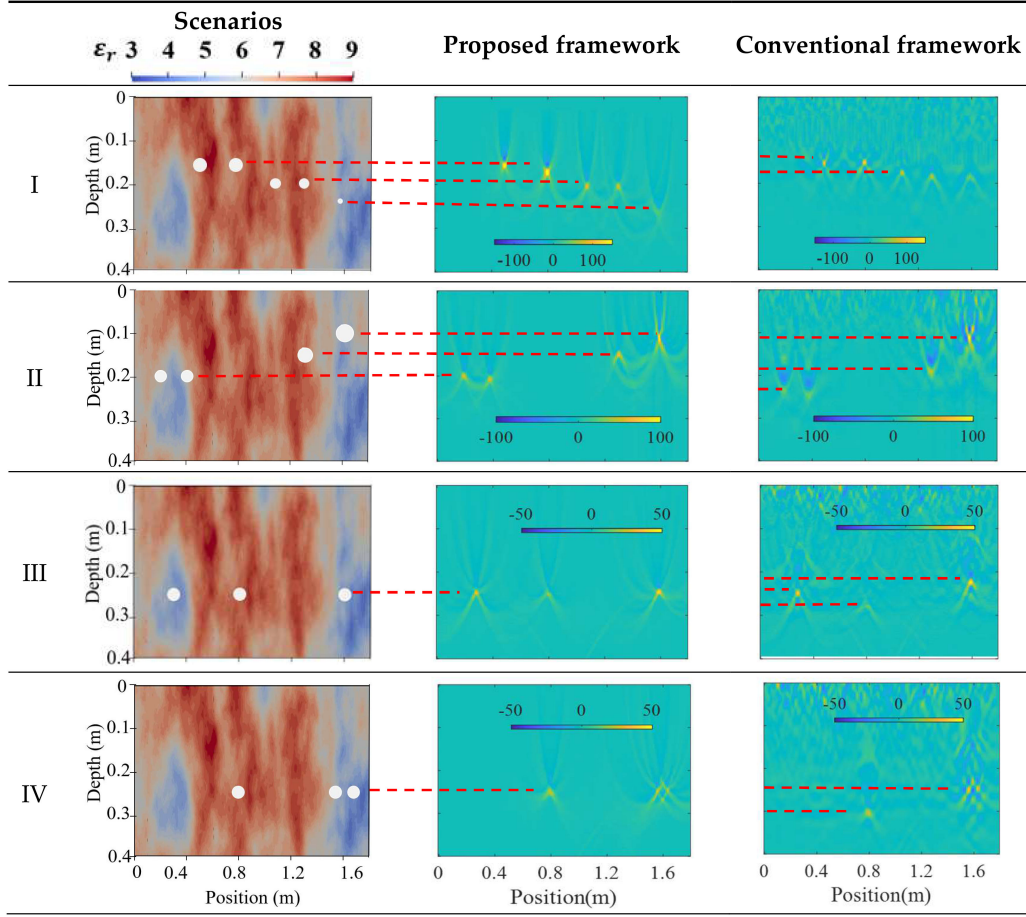


Fig. 14. Comparison of the proposed method and the conventional method in restoring four different root scenarios for the same soil environment.

different soil conditions. From the perspective of image quality, the proposed framework produces clearer images with a high SNR. The conventional framework, however, fails to generate a well-presented image in some cases as the amplitude of the signal from deeply buried fine roots is comparable to the amplitude of the noise, as pointed out in Fig. 13(b). This makes the signal of interest indistinguishable from the noise and causes difficulties in image interpretation.

In addition, four different tree root scenarios in the same soil environment are considered to examine the applicability of the proposed framework for different root scenarios. The B-scans for different scenarios are processed by both the proposed framework and the conventional framework, and the results are illustrated in Fig. 14. For cases I-III, where roots with different radius are located at different places, our framework maintains high accuracy in depth estimation and produces high-quality images with less noise. However, the conventional framework

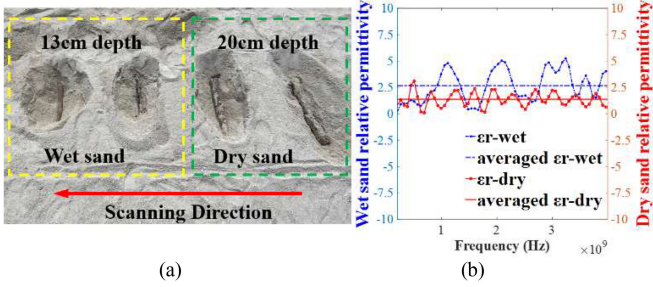


Fig. 15. (a) Four roots buried in sandy soil with different water contents. (b) Relative permittivity of the wet and dry sandy soil measured using the 85070E dielectric probe.

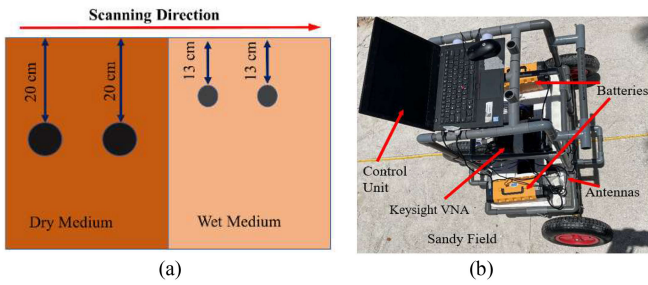


Fig. 16. (a) Side view of the field test site. (b) GPR system used in field tests.

leads to inaccurate depth estimation and generates images with more pronounced noise, such as in case II. For case IV, where two of the three roots are closely placed (the center-to-center distance is less than 10 cm), the image produced by the conventional framework has two focused points interfering with each other, which makes the object differentiation nontrivial. On the contrary, the proposed framework resolves the two closely placed points and eases the image interpretation.

All the results shown in Fig. 14 demonstrate that compared with the conventional framework, the proposed framework achieves a more accurate estimation of the position of each tree root and produces images with greatly reduced noise. The applicability and generalizability of the proposed framework are also verified in different soil and root scenarios.

IV. FIELD EXPERIMENTS

A. Controlled Field Experiment Scenario and Setup

The controlled field experiment was conducted in a controlled environment in our testbed, as shown in Fig. 15(a). The testbed has a size of $4 \times 2 \times 2 \text{ m}^3$ and is filled with heterogeneous sandy soil composed of sand and pebbles. Four cylindrical roots were buried in the field. Two of the roots were positioned at a depth of approximately 20 cm and the other two roots were located at a depth of 13 cm. To enhance the soil's heterogeneity, water is added to a part of the field, as given in Fig. 16(a). The relative permittivity values of dry and wet soil parts were measured using the Agilent 85070E dielectric open-ended coaxial probe, and the results are shown in Fig. 15(b). The wet and dry fields have the biggest relative permittivity of 5.65 and 2.73, respectively. The side view of the scenario is shown as Fig. 16(a).



Fig. 17. (a) Tree under detection. (b) Survey line of the B-scan.

The GPR system consists of a computer-controlled Keysight P5008A vector network analyzer (VNA) as a transceiver and two compact dual-polarized Vivaldi antennas [52], as shown in Fig. 16(b). The antennas are sealed in a Styrofoam box and are installed on a trolley. The two antennas have a 0.1 m separation. The height of antennas above the soil surface is fixed as 0.01 m. Absorbers are placed around the antennas to reduce direct coupling between the antennas and environmental noise. The VNA sweeps 1001 frequency points in the frequency band from 0.4 to 3.4 GHz. The intermediate frequency bandwidth is set as 500 Hz [53], and the power is set as -10 dBm. In the measurement, the two antennas are connected to ports 1 and 2 of the VNA. The antenna polarization is parallel to the object orientation. The transmission coefficient S_{21} is recorded and then transformed to the time domain by IFFTs. 85 A-scans are recorded by moving the GPR system along the preset scanning trace with a step size of 0.035 m. The collected data are further processed using our proposed framework. The experiment is done in the middle of the testbed, the beginning and ending points of the B-scan are half a meter to each side of the testbed, to ensure that there is no reflection from the edges of the test side.

B. Real Tree Root Detection and Setup

The tree roots of an Angsana tree located at $1^{\circ}20'73.3''\text{N}$ $103^{\circ}52'12.2''\text{E}$ is scanned. A photograph of the tree is shown in Fig. 17(a). The tree root system covers an approximate area of $15 \times 15 \text{ m}^2$. Due to the large area and different environment as shown in Fig. 17(a), the soil along the survey line is expected to be heterogeneous. The GPR system used is the same as that used in controlled field experiment in Section IV-A. The survey line is about 6 m, and the spatial step between radar traces is 0.03 m.

C. Controlled Field Experimental Result

First, to eliminate the effects of antenna-to-antenna separation and antenna-to-ground height, the original A-scans are processed by the time-zero correction method. In Fig. 18(a), only oscillations caused by antenna-to-antenna separation and ground reflection are shown when there are no subsurface objects buried. The oscillations after the first peak are the multiple reflections from the ground surface. In Fig. 18(b), the oscillation caused by antenna-to-antenna separation and ground reflection is at the same point as in Fig. 18(a), and there is an obvious positive

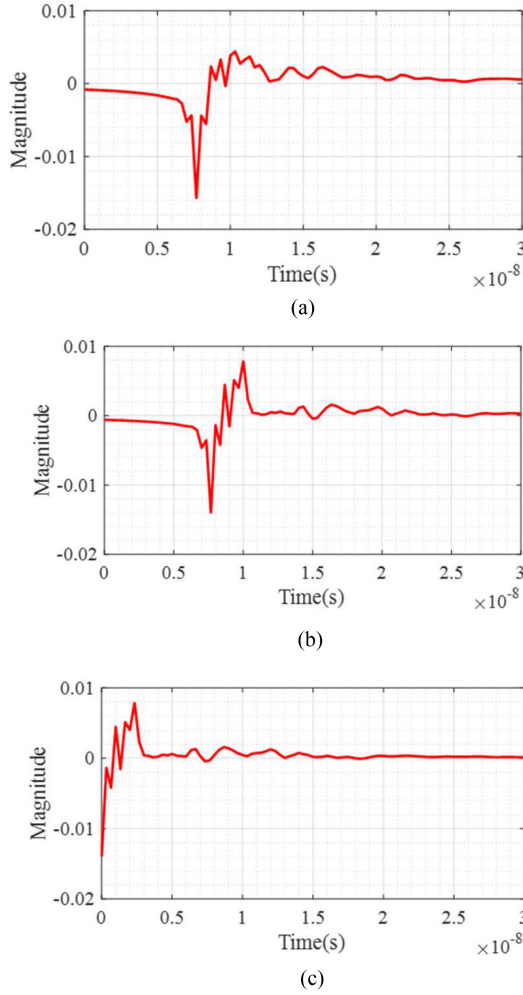


Fig. 18. A-scans of (a) raw data with no reflection from the targets. (b) Raw data with a reflection from the target. (c) Data with reflection from the target through time-zero correction.

peak caused by underground targets reflection. In Fig. 18(c), the A-scan is time-zero corrected by setting the negative maximum point of the ground reflection as the reference time-zero position.

The proposed framework is also applied to process the data collected from the controlled field experiment described in Section IV-A. Fig. 19(a) and (b) shows the time-zero corrected and the preprocessed B-scans, respectively. Four hyperbolae can be identified in the preprocessed B-scan [see Fig. 19(b)]. Based on the proposed framework, the hyperbolae are separated and extracted from the preprocessed B-scan using the C3 technique. Then, the soil equivalent permittivity values of four roots are given in Table IV, together with the estimated depth and horizontal position. The estimated equivalent soil permittivity for root3 and root4 (buried in wet part) is higher than that for root1 and root2 (buried in dry part), which agrees with the field setting well. Using these values accordingly, each root is restored. Finally, all the focused points are combined into a final image, as shown in Fig. 20(a).

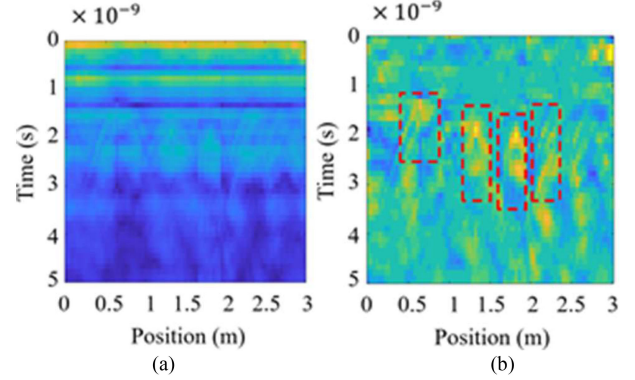


Fig. 19. (a) Raw data after time-zero correction. (b) Preprocessed B-scan via SVD and adaptive thresholding.

TABLE IV
ESTIMATED SOIL EQUIVALENT PERMITTIVITY VALUES, DEPTH, AND HORIZONTAL POSITION FOR EACH ROOT OF THE TEST FIELD BY THE PROPOSED FRAMEWORK

Roots	$\hat{\epsilon}_r$	Estimated Depth	Real Depth	Estimated Horizontal position	Real Horizontal position
Root 1	1.72	0.19	0.20	0.68	0.60
Root 2	2.42	0.19	0.20	1.32	1.30
Root 3	5.42	0.13	0.13	1.82	1.80
Root 4	3.40	0.13	0.13	2.36	2.40

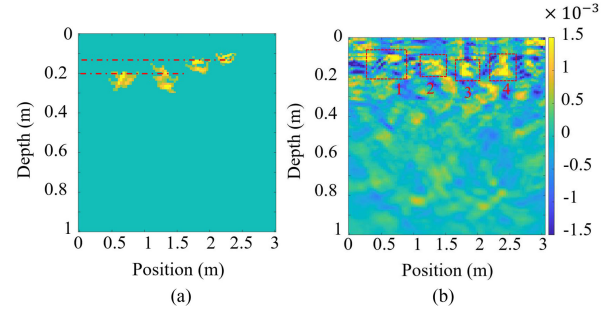


Fig. 20. The reconstructed scenario from (a) the Proposed framework and (b) the conventional framework in which data are processed with constant soil permittivity = 5.02.

By comparing Fig. 20(a) with the result of the conventional framework displayed in Fig. 20(b), it is evident that the proposed framework, which deals with each hyperbola with the corresponding medium equivalent permittivity, can accurately estimates the root depths and significantly reduces the environmental noise in the final image. In terms of position estimation, the RMSREs for the depths and horizontal positions estimated by our proposed framework are 5% and 0.26%, respectively, while RMSRE results for those estimated by using the conventional framework with permittivity $\hat{\epsilon}_{eq} = 5.02$ are 20% and 0.5%, respectively. Besides, in the reconstruction results of Fig. 20(b), the signatures are not focused well, and the depth indication is not accurate due to the incompatible relative permittivity of the surrounding soil. For the result obtained by the conventional framework Fig. 20(b), it is difficult to distinguish the focused signatures of the four roots from the surrounding noises.

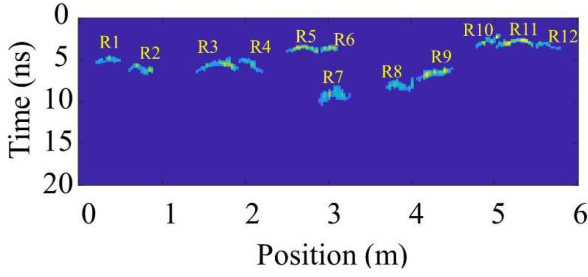


Fig. 21. Hyperbolae radargrams indicating tree roots.

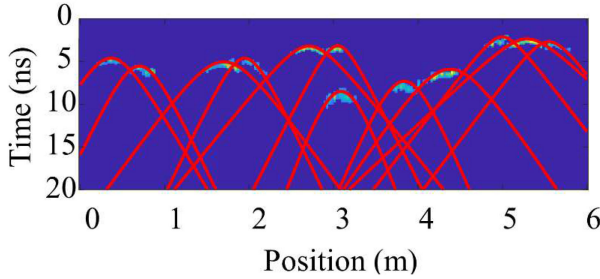


Fig. 22. Fitted hyperbolae of radargrams.

TABLE V
SOIL EQUIVALENT PERMITTIVITY VALUES OF ROOT R1 TO R12

Roots	R1	R2	R3	R4	R5	R6
Equivalent soil permittivity	6.2	10.2	4.5	9.8	8.8	12.4
Roots	R7	R8	R9	R10	R11	R12
Equivalent soil permittivity	8.9	12.8	4.8	4.6	4.0	4.0

D. Real Tree Detection Results

The images plotted in Fig. 21 are the preprocessed raw radargrams. R1 to R12 are hyperbolae extracted by using C3 methods, the hyperbolae indicate radargrams reflected by tree roots.

To estimate the corresponding soil equivalent permittivity of each root, the IHT procedure in the different spatial regions is applied. Especially, for each hyperbola in Fig. 21, the hyperbola fitting process is performed as shown in Fig. 22, the estimated surrounding soil equivalent permittivity of each root is given in Table V. The estimated soil permittivity values cover the interval [4.0, 12.8] over the underground spatial of interest. It is clear to see that the soil permittivity values around roots R1 to R8 are larger than 6, while the values around R9 to R12 are smaller than 5. The estimated permittivity also varies with depth.

The reconstructed image attained by considering the corresponding soil equivalent permittivity of each root is shown in Fig. 23. As it can be observed, the spots that indicate the location of the roots are well focused. The side effect of erroneous modeling of the soil permittivity, which is assumed to be spatially constant, is also investigated. Fig. 24 shows the reconstruction attained by considering the constant soil permittivity equals 12.8. Compared with the image achieved with the root

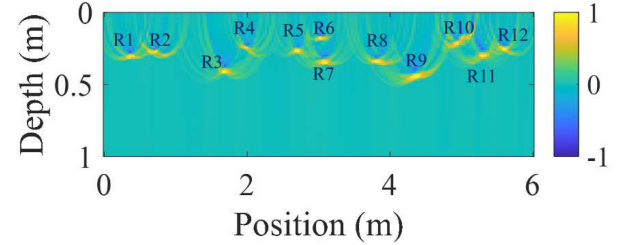


Fig. 23. Reconstructed images that achieved by using the corresponding equivalent soil permittivity value of each root.

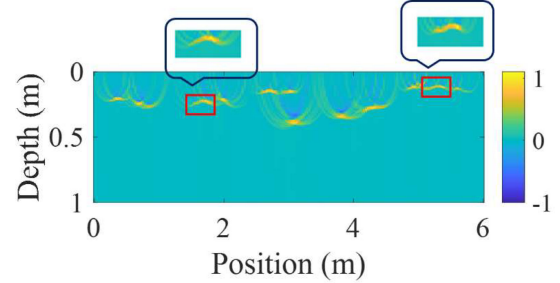


Fig. 24. Reconstructed images that achieved by a constant soil permittivity value equals 12.8.

corresponding soil equivalent permittivity [see Fig. 23], Fig. 24 shows that, although the targets are still detected, they appear defocused along the x-axis and delocalized in depth. To make it clearer, the reconstructed images of R3 and R11 in Fig. 24 are enlarged, the final feature of R3 and R4 are still in hyperbola shape, roots positions are affected since the individual roots cannot be clearly separated and reconstructed for the realistic underground scenario.

V. CONCLUSION

In this article, a signal processing framework for tree roots GPR data in heterogeneous soil environments was proposed to improve the 2-D reconstruction result by taking the variation of the permittivity of the soil into consideration. The proposed framework made use of four main techniques sequentially: A hyperbola separation and extraction method based on the C3 algorithm was implemented to obtain individual hyperbolae and reduce the clutter caused by the soil heterogeneity. An IHT technique was subsequently applied to estimate the soil equivalent permittivity for each hyperbola. The estimated soil equivalent permittivity values are used to further retrieve the root. Finally, all the focalized images are combined into an image to restore the scenario of underground roots. The performance of the proposed framework has been tested using both simulated and measured GPR data under different soil conditions. All the results demonstrate that the proposed framework improves the 2-D tree roots reconstruction result by comparing with the result of the conventional frameworks that treating soil permittivity as a constant. Furthermore, the framework can improve the detection accuracy of the tree roots regardless of the soil heterogeneity and root distribution, which facilitates tree root mapping in realistic soil environments.

REFERENCES

- [1] R. K. Dixon, A. Solomon, S. Brown, R. Houghton, M. Trexier, and J. Wisniewski, "Carbon pools and flux of global forest ecosystems," *Science*, vol. 263, no. 5144, pp. 185–190, 1994.
- [2] A. Fitter, "Characteristics and functions of root systems," *Plant Roots, Hidden Half*, vol. 3, pp. 15–32, 1996.
- [3] R. B. Jackson, H. A. Mooney, and E.-D. Schulze, "A global budget for fine root biomass, surface area, and nutrient contents," *Proc. Nat. Acad. Sci.*, vol. 94, no. 14, pp. 7362–7366, 1997.
- [4] A. Brookes, "Preventing death and serious injury from falling trees and branches," *J. Outdoor Environ. Educ.*, vol. 11, no. 2, pp. 50–59, 2007.
- [5] R. J. Norby and R. B. Jackson, "Root dynamics and global change: Seeking an ecosystem perspective," *New Phytologist*, vol. 147, no. 1, pp. 3–12, 2000.
- [6] A. Pierret, C. J. Moran, and C. Doussan, "Conventional detection methodology is limiting our ability to understand the roles and functions of fine roots," *New Phytologist*, vol. 166, no. 3, pp. 967–980, 2005.
- [7] L. He, S. Ji, W. R. Scott, and L. Carin, "Adaptive multimodality sensing of landmines," *IEEE Trans. Geosci. Remote Sens.*, vol. 45, no. 6, pp. 1756–1774, Jun. 2007.
- [8] R. Firoozabadi, E. L. Miller, C. M. Rappaport, and A. W. Morgenthaler, "Subsurface sensing of buried objects under a randomly rough surface using scattered electromagnetic field data," *IEEE Trans. Geosci. Remote Sens.*, vol. 45, no. 1, pp. 104–117, Jan. 2006.
- [9] J. R. Butnor, J. Doolittle, L. Kress, S. Cohen, and K. H. Johnsen, "Use of ground-penetrating radar to study tree roots in the Southeastern United States," *Tree Physiol.*, vol. 21, no. 17, pp. 1269–1278, 2001.
- [10] M. Dannoura *et al.*, "Detection of Cryptomeria japonica roots with ground penetrating radar," *Plant Biosyst.*, vol. 142, no. 2, pp. 375–380, 2008.
- [11] H.-H. Sun, Y. H. Lee, W. Luo, L. F. Ow, M. L. M. Yusof, and A. C. Yucel, "Dual-cross-polarized GPR measurement method for detection and orientation estimation of shallowly buried elongated object," *IEEE Trans. Instrum. Meas.*, vol. 70, pp. 1–12, 2021, Art no. 8004912, doi: 10.1109/TIM.2021.3116292.
- [12] J. R. Butnor, J. Doolittle, K. H. Johnsen, L. Samuelson, T. Stokes, and L. Kress, "Utility of ground-penetrating radar as a root biomass survey tool in forest systems," *Soil Sci. Soc. Amer. J.*, vol. 67, no. 5, pp. 1607–1615, 2003.
- [13] X. Cui, J. Chen, J. Shen, X. Cao, X. Chen, and X. Zhu, "Modeling tree root diameter and biomass by ground-penetrating radar," *Sci. China Earth Sci.*, vol. 54, no. 5, pp. 711–719, 2011.
- [14] S. Lauro *et al.*, "Electromagnetic signal penetration in a planetary soil simulant: Estimated attenuation rates using GPR and TDR in volcanic deposits on Mount Etna," *J. Geophys. Res., Planets*, vol. 122, no. 7, pp. 1392–1404, 2017.
- [15] R. Yelf, "Where is true time zero?," in *Proc. 10th Int. Conf. Grounds Penetrating Radar*, 2004, vol. 1, pp. 279–282.
- [16] A. Annan, "Ground-penetrating radar," in *Near-Surface Geophysics*: Houston, TX, USA: Soc. Exploration Geophysicists, 2005, pp. 357–438.
- [17] P. X. Neto and W. E. de Medeiros, "A practical approach to correct attenuation effects in GPR data," *J. Appl. Geophys.*, vol. 59, no. 2, pp. 140–151, 2006.
- [18] R. Persico and F. Soldovieri, "Effects of background removal in linear inverse scattering," *IEEE Trans. Geosci. Remote Sens.*, vol. 46, no. 4, pp. 1104–1114, Apr. 2008.
- [19] G. Chen and S.-E. Qian, "Denoising of hyperspectral imagery using principal component analysis and wavelet shrinkage," *IEEE Trans. Geosci. Remote Sens.*, vol. 49, no. 3, pp. 973–980, Mar. 2010.
- [20] A. De Coster and S. Lambot, "Full-wave removal of internal antenna effects and antenna–medium interactions for improved ground-penetrating radar imaging," *IEEE Trans. Geosci. Remote Sens.*, vol. 57, no. 1, pp. 93–103, Jan. 2019.
- [21] L. Mertens, R. Persico, L. Matera, and S. Lambot, "Automated detection of reflection hyperbolas in complex GPR images with no a priori knowledge on the medium," *IEEE Trans. Geosci. Remote Sens.*, vol. 54, no. 1, pp. 580–596, Jan. 2016.
- [22] L. Lantini, F. Tosti, I. Giannakis, L. Zou, A. Benedetto, and A. M. Alani, "An enhanced data processing framework for mapping tree root systems using ground penetrating radar," *Remote Sens.*, vol. 12, no. 20, 2020, Art. no. 3417.
- [23] A. Aboudourib, M. Serhir, and D. Lesselier, "A processing framework for tree-root reconstruction using ground-penetrating radar under heterogeneous soil conditions," *IEEE Trans. Geosci. Remote Sens.*, vol. 59, no. 1, pp. 208–219, Jan. 2021.
- [24] S. Lameri, F. Lombardi, P. Bestagini, M. Lualdi, and S. Tubaro, "Landmine detection from GPR data using convolutional neural networks," in *Proc. 25th Eur. Signal Process. Conf.*, 2017, pp. 508–512.
- [25] M. A. González-Huici, I. Catapano, and F. Soldovieri, "A comparative study of GPR reconstruction approaches for landmine detection," *IEEE J. Sel. Topics Appl. Earth Observ. Remote Sens.*, vol. 7, no. 12, pp. 4869–4878, Dec. 2014.
- [26] G. Gennarelli, I. Catapano, X. Dérobert, and F. Soldovieri, "A ground penetrating radar imaging approach for a heterogeneous subsoil with a vertical permittivity gradient," *IEEE Trans. Geosci. Remote Sens.*, vol. 59, no. 7, pp. 5698–5710, Jul. 2021.
- [27] A. Bitri and G. Grandjean, "Frequency–wavenumber modelling and migration of 2D GPR data in moderately heterogeneous dispersive media [Link]," *Geophys. Prospecting*, vol. 46, no. 3, pp. 287–301, 2008.
- [28] M. C. Dobson, F. T. Ulaby, M. T. Hallikainen, and M. A. El-Rayes, "Microwave dielectric behavior of wet soil—Part II: Dielectric mixing models," *IEEE Trans. Geosci. Remote Sens.*, vol. GE-23, no. 1, pp. 35–46, Jan. 1985.
- [29] N. R. Peplinski, F. T. Ulaby, and M. C. Dobson, "Dielectric properties of soils in the 0.3–1.3-GHz range," *IEEE Trans. Geosci. Remote Sens.*, vol. 33, no. 3, pp. 803–807, May 1995.
- [30] Q. Dou, L. Wei, D. R. Magee, and A. G. Cohn, "Real-time hyperbola recognition and fitting in GPR data," *IEEE Trans. Geosci. Remote Sens.*, vol. 55, no. 1, pp. 51–62, Jan. 2016.
- [31] W. Li, X. Cui, L. Guo, J. Chen, X. Chen, and X. Cao, "Tree root automatic recognition in ground penetrating radar profiles based on randomized hough transform," *Remote Sens.*, vol. 8, no. 5, p. 430, 2016.
- [32] X. Liu *et al.*, "Non-invasive estimation of root zone soil moisture from coarse root reflections in ground-penetrating radar images," *Plant Soil*, vol. 436, no. 1, pp. 623–639, 2019.
- [33] C. G. Windsor, L. Capineri, and P. Falorni, "A data pair-labeled generalized hough transform for radar location of buried objects," *IEEE Geosci. Remote Sens. Lett.*, vol. 11, no. 1, pp. 124–127, Jan. 2014.
- [34] J. Gazdag, "Wave equation migration with the phase-shift method," *Geophysics*, vol. 43, no. 7, pp. 1342–1351, 1978.
- [35] W. A. Schneider, "Integral formulation for migration in two and three dimensions," *Geophysics*, vol. 43, no. 1, pp. 49–76, 1978.
- [36] R. H. Stolt, "Migration by Fourier transform," *Geophysics*, vol. 43, no. 1, pp. 23–48, 1978.
- [37] A. Ribalta and M. A. Gonzalez-Huici, "Backprojection algorithm for subsurface radar imaging: Computing the round-trip time delay," in *Proc. IEEE Int. Geosci. Remote Sens. Symp.*, 2013, pp. 1403–1405.
- [38] J. Fortuny-Guasch, "A novel 3-D subsurface radar imaging technique," *IEEE Trans. Geosci. Remote Sens.*, vol. 40, no. 2, pp. 443–452, Feb. 2002.
- [39] E. Pettinelli *et al.*, "GPR response from buried pipes: Measurement on field site and tomographic reconstructions," *IEEE Trans. Geosci. Remote Sens.*, vol. 47, no. 8, pp. 2639–2645, Aug. 2009.
- [40] S. E. Lauro *et al.*, "Estimation of subsurface dielectric target depth for GPR planetary exploration: Laboratory measurements and modeling," *J. Appl. Geophys.*, vol. 93, pp. 93–100, 2013.
- [41] Ö. Yilmaz, *Seismic Data Analysis*. Houston, TX, USA: Soc. Exploration Geophysicists Tulsa, 2001.
- [42] D. J. Daniels, *Ground Penetrating Radar*. IET, London, U.K., 2004.
- [43] X. Feng, M. Sato, and C. Liu, "Hand-held GPR imaging using migration for irregular data," *IEEE J. Sel. Topics Appl. Earth Observ. Remote Sens.*, vol. 4, no. 4, pp. 799–803, Dec. 2011.
- [44] X. Feng, M. Sato, C. Liu, and Y. Zhang, "Profiling the rough surface by migration," *IEEE Geosci. Remote Sens. Lett.*, vol. 6, no. 2, pp. 258–262, Apr. 2009.
- [45] H. Jung, W. Kang, and K. Kim, "Multilayer stolt migration algorithm for subsurface target imaging in oblique layers," *IEEE J. Sel. Topics Appl. Earth Obsrv. Remote Sens.*, vol. 10, no. 10, pp. 4295–4303, Oct. 2017.
- [46] C. Warren, A. Giannopoulos, and I. Giannakis, "gprMax: Open source software to simulate electromagnetic wave propagation for ground penetrating radar," *Comput. Phys. Commun.*, vol. 209, pp. 163–170, 2016.
- [47] A. Paz, E. Thorin, and C. Topp, "Dielectric mixing models for water content determination in woody biomass," *Wood Sci. Technol.*, vol. 45, no. 2, pp. 249–259, 2011.

- [48] J. Straube, D. Onysko, and C. Schumacher, "Methodology and design of field experiments for monitoring the hydrothermal performance of wood frame enclosures," *J. Thermal Envelope Build. Sci.*, vol. 26, no. 2, pp. 123–151, 2002.
- [49] I. Giannakis, A. Giannopoulos, and N. Davidson, "Realistic modelling of ground penetrating radar for landmine detection using FDTD," in *Proc. 15th Int. Conf. Ground Penetrating Radar*, 2014, pp. 954–959.
- [50] I. Giannakis, A. Giannopoulos, and C. Warren, "A realistic FDTD numerical modeling framework of ground penetrating radar for landmine detection," *IEEE J. Sel. Topics Appl. Earth Observ. Remote Sens.*, vol. 9, no. 1, pp. 37–51, Jan. 2015.
- [51] M. Danos, *Fractals and Chaos in Geology and Geophysics*. Hoboken, NJ, USA: Wiley, 1998.
- [52] H.-H. Sun, Y. H. Lee, W. Luo, L. F. Ow, M. L. M. Yusof, and A. C. Yucel, "Compact dual-polarized vivaldi antenna with high gain and high polarization purity for GPR applications," *Sensors*, vol. 21, no. 2, p. 503, 2021.
- [53] W. Luo, H.-H. Sun, Y. H. Lee, A. C. Yucel, G. Ow, and M. L. M. Yusof, "Effects of intermediate frequency bandwidth on stepped frequency ground penetrating radar," in *Proc. IEEE North Amer. Radio Sci. Meeting (Joint AP-S Symp.)*, 2020, pp. 95–96.



Wenhao Luo (Student Member, IEEE) received the B.Eng. degree in automation from Hohai University, Nanjing, China, in 2016, and the M.Sc. degree in electronics engineering in 2019 from the School of Electrical and Electronics Engineering, Nanyang Technological University, Singapore, where he is currently working toward the Ph.D. degree in engineering.

His research interests include the ground penetrating radar, remote sensing techniques, radar signal processing and machine learning techniques.



Yee Hui Lee (Senior Member, IEEE) received the B.Eng. (Hons.) and M.Eng. degrees from the School of Electrical and Electronics Engineering, Nanyang Technological University, Singapore, in 1996 and 1998, respectively, and the Ph.D. degree from the University of York, York, U.K., in 2002.

Since 2002, she has been a Faculty Member with Nanyang Technological University, where she is currently an Associate Professor with the School of Electrical and Electronic Engineering. Her research interests include the channel characterization, rain propagation, antenna design, electromagnetic bandgap structures, and evolutionary techniques.



Hai-Han Sun received the bachelor's degree in electronic information engineering from the Beijing University of Posts and Telecommunications, Beijing, China, in 2015, and the Ph.D. degree in engineering from the University of Technology Sydney, Ultimo, NSW, Australia, in 2019.

She is currently a Research Fellow with the School of Electrical and Electronic Engineering, Nanyang Technological University, Singapore. Her research interests include base station antennas and ground penetrating radar.



of environment.

Lai Fern Ow received the B.S. degree (Hons.) in plant biology from Massey University, Palmerston North, New Zealand, in 2004, and the Ph.D. degree in plant biology from the University of Canterbury, Christchurch, New Zealand, in 2009.

She is currently the Deputy Director with the Centre for Urban Greenery and Ecology, National Parks Board, Singapore. Her research interests include eco-physiology of resource acquisition in urban ecosystems, tree biology/arboriculture, urban sustainability, plant physiology, and responses of plants to extremes



Mohamed Lokman Mohd Yusof received the B.S. degree in biomedical science from the University of Western Australia, Crawley, WA, Australia.

He is currently an Executive with the Centre for Urban Greenery and Ecology, National Parks Board, Singapore. His research interests include arboriculture, remote sensing, and phytoremediation.



Abdulkadir C. Yucel (Senior Member, IEEE) received the B.S. degree in electronics engineering (*summa cum laude*) from the Gebze Institute of Technology, Kocaeli, Turkey, in 2005, and the M.S. and Ph.D. degrees in electrical engineering from the University of Michigan, Ann Arbor, MI, USA, in 2008 and 2013, respectively.

From September 2005 to August 2006, he was a Research and a Teaching Assistant with the Gebze Institute of Technology, Gebze, Turkey. From August 2006 to April 2013, he was a Graduate Student Research Assistant with the University of Michigan, Ann Arbor, MI, USA. Between May 2013 and December 2017, he was a Postdoctoral Research Fellow at various institutes, including the Massachusetts Institute of Technology. Since 2018, he has been an Assistant Professor with the School of Electrical and Electronic Engineering, Nanyang Technological University, Singapore.

Dr. Yucel was the recipient of the Fulbright Fellowship in 2006, Electrical Engineering and Computer Science Departmental Fellowship of the University of Michigan in 2007, and Student Paper Competition Honorable Mention Award at IEEE INTERNATIONAL SYMPOSIUM ON ANTENNAS AND PROPAGATION in 2009. He has been an Associate Editor for *International Journal of Numerical Modelling: Electronic Networks, Devices and Fields* and as a Reviewer for various technical journals.